NDT&E International 137 (2023) 102812

Contents lists available at ScienceDirect

NDT and E International

journal homepage: www.elsevier.com/locate/ndteint

Thermal compensation of ultrasonic transmit and receive data for steel welded plates at the point of manufacture

Euan A. Foster *, Nina E. Sweeney, Ewan Nicolson, Jonathan Singh, Muhammad K. Rizwan, David Lines, Gareth Pierce, Ehsan Mohseni, Anthony Gachagan, Katherine M.M. Tant, Charles N. MacLeod

University of Strathclyde, 16 Richmond St, Glasgow, G1 1XQ, UK

ARTICLE INFO

Keywords:
Ultrasonics
Arrays
Total focusing method
Fast marching method
Weld inspection
In-process inspection
Inspection at the point of manufacture

ABSTRACT

On modern manufacturing production lines, Non-Destructive Testing (NDT) is frequently a bottleneck which could greatly be alleviated by integrating the inspection of components as they are manufactured. By moving inspection to the point of manufacture, greater economic and productivity benefits are realised in terms of reduced rework and schedule slippage, however, new technical challenges emerge. For welded components, high temperatures and the resulting thermal gradients, present challenges when performing ultrasonic inspection at the point of manufacture. The thermal gradients introduce positional misalignment due to "beam bending" effects arising from refraction as the material properties change with temperature. This paper presents for the first time, through simulation and practical experiments, a novel thermal compensation strategy to mitigate for thermal effects when performing ultrasonic inspection of welded components at the point of manufacture. To understand the thermal gradients experienced during standard Tungsten Inert Gas (TIG) welding, 3-dimensional thermal simulations were developed and experimentally-validated with an average error of 1.80% (mean error: 4.1°C, max error: 19.2°C). The output from the thermal simulations in combination with material properties that vary over temperature, allowed for generalised time of flight maps to be created via the Multi-Stencils Fast Marching Method (MSFMM) and the ultrasonic data to be imaged by the Total Focusing Method (TFM). The thermal compensation strategy was initially proved on synthetically generated finite element Full Matrix Capture (FMC) datasets, and it was shown that reflector positional accuracy could be increased by ~ 3 mm. Experimental results also showed marked improvements with reflector positional accuracy also being increased by ~3 mm. Over both simulated and experimental datasets, the SNR was shown to be negligibly altered between uncompensated and compensated images. The results show how high-quality ultrasonic images can be generated in-process and help bring inspection closer to the point of manufacture.

1. Introduction

Ultrasonic phased arrays have become increasingly popular in many Non-Destructive Testing (NDT) applications due to their flexibility, quality, and reduced inspection times [1,2]. Flexibility in the acquisition of data is ensured since the same array can be used for various differing inspections, while flexibility in post-processing arises from the variety of imaging algorithms that can be applied to the rich ultrasonic datasets acquired by arrays. Advanced array data acquisition strategies, including Full Matrix Capture (FMC) [3] and plane wave [4], have enabled various images to be generated through algorithms, such as the Total Focusing Method (TFM) [5], Phase Coherence Imaging (PCI) [6], the wavenumber algorithm [7], and Inverse Wave Field Extrapolation (IWEX) [8], and have allowed for optimised geometries and features to be detected.

FMC datasets, where a complete set of time domain A-scan data is acquired from all combinations of transmit/receive elements, have widely become the *de facto* standard to which imaging algorithms are applied [3]. It is necessary for these imaging algorithms to incorporate some element of *a priori* knowledge in order to accurately detect and characterise any present defects. One such imaging algorithm is the TFM [5]. In the TFM, *a priori* knowledge of the ultrasonic velocity within the component is used in a forward model to create a Time of Flight (ToF) map from each transmit/receive pair to each pixel in the imaging

* Corresponding author.
E-mail address: e.foster@strath.ac.uk (E.A. Foster).

https://doi.org/10.1016/j.ndteint.2023.102812
Received 30 August 2022; Received in revised form 28 November 2022; Accepted 5 February 2023
Available online 8 February 2023

domain. The amplitude corresponding to each of the times in the ToF map is extracted, and the results from every transmit/receive pair in the FMC dataset are then summed. This creates an image that is synthetically focused across the entire domain, leading to increased defect detection and improved characterisation [9–12]. Furthermore, as the cost of array electronics continues to decrease and the speed of computation increases, FMC acquisition and TFM imaging is becoming more widespread.

There have been various adaptations of the TFM algorithm from the basic single domain embodiment described in the previous paragraph. Recent innovations include: 1) adapting FMC acquisition and TFM imaging for laser induced ultrasound [13–15]; 2) introducing iterative "ray tracing" algorithms in the forward model to calculate the required ToF maps for multiple material layers [16,17] and anisotropic materials [18,19], as well as; 3) incorporating "path finding" algorithms [20–22] in the forward model to likewise calculate complex ToF maps. Many industrially relevant applications are realised by the expansion of TFM imaging to multiple material layers and anisotropic materials, especially in relation to the in-process inspection of challenging multi-pass weld geometries [23] and Wire Arc Additive Manufactured (WAAM) components [24–26]. Ray tracing algorithms typically rely on an iterative solution of the wave equation via Fermat's principle of minimum time to generate a ray path and subsequent ToF map. Due to their iterative nature, these algorithms have been shown in the literature to be computationally demanding [20] and as a result slow. In order to address these issues, path finding algorithms, that have their origin in computer science [27–29], have been introduced to great effect. Tant et al. [21,22] & Bourne et al. [30] have demonstrated that by deploying path finding algorithms, the grain orientation maps for anisotropic media can be efficiently determined. More recently, Singh et al. [31] demonstrated that Finite Element (FE) datasets in combination with path finding algorithms can be used to train deep learning models to enable real time inversion of microstructural maps.

It is well documented how temperature can affect the ultrasonic velocity within a component made from a specific material [32], and how thermal effects can pose challenges when characterising defects [33–37]. A thermal gradient within a component can be regarded as a multi layered or anisotropic component with each thermal zone being a different material or phase in the component. These different thermal zones introduce "beam bending" effects arising from refraction and represent some of the hardest inspection scenarios in ultrasonic imaging. The usual *a priori* assumption utilised in imaging algorithms of the ultrasonic velocity being constant within the domain is therefore invalid and needs to be addressed for imaging algorithms to allow for in-process inspection. These challenging environments are encountered at the point of manufacture for multi-pass welded components. Due to the challenges associated with inspecting at temperature, industry standards dictate that inspection is carried out after the final deposition and when the sample has cooled to ambient temperature [38–40]. This approach makes correcting any defects found post manufacture more complex and expensive, with delays contributing to uncertainty in the manufacturing schedule, with scrapping of the entire component not being uncommon [41,42]. As businesses shift towards Industry 4.0, there is a demand for automated integration of inspection within the manufacturing process [43]. If inspection of multi-pass welded components were to be performed in-process at the point of manufacture, huge economic benefits would be realised in being able to rectify for defects earlier in the manufacturing process, optimising production volumes, and decreasing lead times. Overcoming these challenges and providing high resolution ultrasonic images of welds at the point of manufacture is therefore highly desirable for many industrial sectors, such as nuclear, aerospace, defence, and oil and gas, where welds play a critical role.

In this paper, we present the theoretical approach and experimental verification for the correction of the thermal effects observed in ultrasonic imaging of welded components at the point of manufacture.

Initially, accurate FE simulations of the thermal environment which mimicked the Tungsten Inert Gas (TIG) weld procedure specification of a 21-pass, 7-layer, 16 mm thick S275 carbon steel weld with a 90° included bevel were created. This thermal dataset was then verified through extensive experimentation in a flexible robotic cell which automatically performed the weld procedure [35,44,45] and logged the temperature over time using 13 K-type thermocouples through a National Instruments 9214 temperature module [46]. The results demonstrated that the simulated dataset was in excellent alignment with the experimental thermocouple data with an average error of 1.80% (mean error: 4.1°C, max error: 19.2°C).

With confidence that the simulated thermal data across the full domain was valid and accurate, several 2D ultrasonic FE models were created that produced FMC data representative of a Commercial Off The Shelf (COTS) 64-element array. The FE model domain comprised: an inhomogeneous steel welded plate that allowed for variations in the ultrasonic velocity with a single reflector present in the centre of the weld; a wedge typically used in weld inspection; and absorbing regions to limit the domain size. By using the well documented material properties of S275 steel that vary over temperature, differing thermal zones were able to be replicated within the FE models [47,48]. The Multi-Stencils Fast Marching Method (MSFMM), a path finding algorithm, was then deployed to compute the necessary ToF maps for the TFM algorithm [49]. It was shown that by compensating for thermal gradients in the simulated datasets, the reflector's indication positional error was reduced by ~3 mm while the focusing performance was negligibly altered. A positional shift of this magnitude is in the order of a weld pass width and thickness which would change the required rework operation to remedy. This result demonstrates the efficacy of the proposed thermal compensation scheme as accurate and fast detection is key for partially filled weld geometries associated with in-process inspection.

Experimental validation was achieved via an autogenous weld being applied to a 15.8 mm thick S275 carbon steel plate with two 2 mm Side-Drilled Hole reference reflectors positioned to match the fusion interface. The experimental results showed that performing thermal compensation produced no meaningful difference in SNR, but the positional error was reduced by ~3 mm. The results presented in this study show a significant step towards industrially desirable inspection at the point of manufacture.

2. Methodology

The exchange of information that underpins the flow of this article is depicted in Fig. 1. An overview of the theory underpinning the TFM and the MSFMM is given in Section 2.1 & 2.2 respectively. Further details are then provided for thermal validation (Section 3), ultrasonic simulations (Section 4), as well as the experimental validation (Section 5).

2.1. Total Focusing Method

The TFM is a standard imaging algorithm for detecting and characterising defects used widely across the NDT community. TFM uses the FMC dataset, consisting of recorded signals, referred to as A-scans, transmitted at each element of an ultrasonic array, s_{xy}, and received at all elements of the ultrasonic array, $r_{x,y}$, over time, t. Each recorded A-scan can therefore be denoted as $A_{s_{xy}r_{xy}}(t)$.

Conventional TFM algorithms assume a constant wave speed, c, throughout the entire domain, and calculates the distances from each transmitting element, s_{xy}, to each receiving element, $r_{x,y}$, to every imaging point. With the distance and speed known, this enables the calculation of the travel times in the imaging domain and be related to an amplitude in the corresponding A-scan. The intensity of each pixel in the TFM imaging domain, $I(x_i,y_i)$, is the sum of all amplitudes in each A-scan of the FMC dataset. This is mathematically described in Eq. (1), where x_{s_x} and y_{s_y} are the x and y coordinates of the transmitting

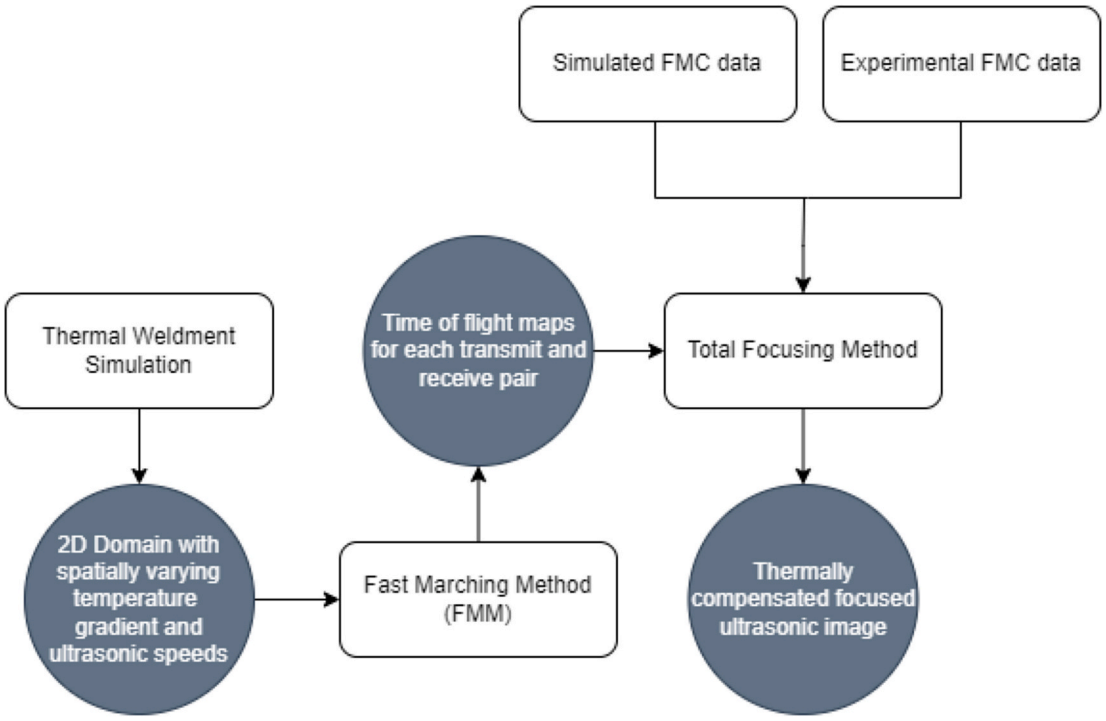

Fig. 1. Flowchart showing the various modelling techniques and algorithms used within this study.

ultrasonic array element, and x_{r_x} and y_{r_y} are the x and y coordinates of the receiving ultrasonic array element.

$$I(x_i,y_i)=\left|\sum_{s_{x,y}=1}^{N} \times \sum_{s_{x,y}=1}^{N} A_{s_{x,y}r_{x,y}}\left(\frac{\left(\sqrt{(x_{s_x}-x_i)^2+\left(y_{s_y}-y_j\right)^2}+\sqrt{(x_{r_x}-x_i)^2+\left(y_{r_y}-y_j\right)^2}\right)}{c}\right)\right| \quad \text{Eq. 1}$$

The mathematical description contained within Eq. (1), is accurate for an isotropic domain which has constant material properties that are spatially invariant. As alluded to previously, an isotropic material in the presence of a thermal gradient introduces spatial variations in the ultrasonic velocity as a function of the applied thermal gradient. It is therefore necessary to incorporate an approach where the simplistic geometric forward model is replaced with one that is more complex and can account for spatial changes in material properties. This generalised ToF map could be calculated by any forward modelling technique, however, for this study, the MSFMM was used to compute the required ToF maps. Implementation of the TFM algorithm in conjunction with the MSFMM has been previously referred to as TFM+ in previously published work [21,22]. By using the MSFMM in this manner, it can be said that for an array of N elements, N ToF maps are generated from each source to each pixel in the domain. Assuming a pulse-echo set-up, source-receiver reciprocity can be invoked, where the travel time for a wave to travel from each transmitting element to each pixel can be assumed to be the same as the travel time from each pixel to each receiving element. Therefore, the TFM image intensity can be calculated through Eq. (2) with the introduction of, τ, to represent a generalised ToF map. This generalised ToF map is expanded upon in Section 2.2 and is formally documented within Eq. (3).

$$I(x_i,y_i)=\left|\sum_{s_{x,y}=1}^{N}\sum_{s_{x,y}=1}^{N} A_{s_{x,y}r_{x,y}}(\tau_s(x_i.y_i)+\tau_r(x_i.y_i))\right| \quad \text{Eq. 2}$$

2.2. Multi-Stencils Fast Marching Method

To calculate the travel times through spatially varying medium, forward model must be used. The MSFMM is used in this study as the forward model to simulate the wave front propagation in the heterogenous steel domain and to provide accurate estimates of travel times, accounting for the varying velocities and resulting wave refraction caused by the presence of thermal gradients. The MSFMM is an adaptation of the original Fast Marching Method (FMM) first proposed in Ref. [49] for generating computational solutions to the nonlinear Eikonal equation, and by extension related static Hamilton-Jacobi equations. FMMs make use of entropy satisfying upwind schemes and fast sorting techniques to produce highly accurate, repeatable, and efficient results. The traditional FMM has been shown to be inaccurate along diagonal trajectories on coarsely discretised domains as only the nearest neighbours in each node are considered. As the wavefront propagates through the discretised domain, errors accumulate and compound along the directions between axis vectors. To avoid this issue, the MSFMM [50] is used in this study which adds the diagonals to the shortest time calculation by performing a 45° rotation to the original four-point stencil. This higher order fast marching method (on which MSFMM is based) has been shown to diminish the grid bias and converge to the underlying geodesic distance when the grid step size tends to zero [51]. Various differing embodiments of the MSFMM have been developed and successfully been deployed in similar studies to account for refraction in isotropic [21] and anisotropic media [22]. For this study, only spatially-varying isotropic media is considered.

The MSFMM solves the Eikonal equation stated in Eq. (3). $\tau(x_i,y_i,s_{xy})$ denotes the minimum travel time for a wave to travel from the transmitter $s \in \partial I$, on the boundary of the discretised image domain $I = x \times y$, to the point $(x_i,y_i) \in I$. An upwind finite difference scheme is used to solve for $\Delta\tau(x_i,y_i,s_{xy})$ [52], where $V(x_i,y_i)$ is the velocity model depicting the velocity at point (x_i,y_i).

$$\left|\Delta\tau\left(x_i, y_i, s_{xy}\right)\right| = \frac{1}{V(x_i, y_i)} \quad \text{Eq. 3}$$

Solving Eq. (3) over a regular grid with an associated velocity field, the shortest travel-time between each transmitter, $s_{x,y}$ and receiver $r_{x,y} \in \partial I$ can be calculated, and the travel time matrix constructed. It is noted that other physical phenomena such as scattering, attenuation and dispersion are ignored and only the travel time information is modelled. FMM algorithms such as the MSFMM have been shown to be an efficient, robust, and fast method for computing travel times for complex spatially-varying media [53]. Thus, imaging techniques, like TFM, that require a time-of-flight for many pixels in an imaging domain, prosper from the use of such an algorithm. A more thorough theoretical overview of the MSFMM is outside the scope of this paper but readers are referred to Hassouna & Farag [50] for further information and discourse.

3. Thermal simulation

In order to quantify the thermal gradients that could be experienced during in-process inspection, several 3D thermal simulations of a 21 pass, 7-layer, 16 mm thick carbon steel S275 weld with a 90° included bevel were performed in the commercial FE package, COMSOL [54]. A total of 7 models were produced to mimic the thermal gradient observed for each layer during a TIG welding process. An ambient convection and radiation boundary condition was applied of 20 °C at the surface of the steel for all models. The steel was modelled with a specific heat capacity of 475 $\frac{J}{kgK}$ and a thermal conductivity of 44.5 $\frac{W}{mK}$. Each model domain was 600 × 16 × 400 mm, comprised ~15,605 tetrahedral elements and is shown in Fig. 2.

Experimental verification of the simulations was undertaken in tandem. Two steel plates 300 × 16 × 400 mm in size with a 90° included bevel were fabricated as shown in Fig. 3 (a). The weld procedure is documented in Fig. 3 (b) with each pass sequentially numbered. Pass 1 and 2 refers to layers 1 and 2 respectively, while passes 3–4, 5–7, 8–11, 12–16, 17–21 refer to layers 3, 4, 5, 6 & 7, respectively.

A total of 13 K-type thermocouples were attached to the plates prior to welding. Seven were attached to the upper surface of the left-hand plate and six were attached to the bottom of the right-hand plate, as shown in Fig. 3 (c) & (d). For the last pass in each layer, the temperature was recorded for a total of 380 s.

A robotic cell as described in previously published work was used to automatically perform the welding procedure [44,45]. For all passes performed by the robotic system, the welding parameters documenting the welding current, voltage, travel speed, weave amplitude and frequency are given in Table 1.

After each layer, a laser scan with a 2910-100 Micro-Epsilon laser scanner [55] was performed to document each layers geometry. These scanned cross sections were used to generate CAD models for the thermal simulations and are shown in Fig. 4. It is also important to note that in between each pass, the plates were allowed to cool to ambient with a mean cool down time of 30-40 mins depending on the pass number and location as well as the welding parameters. This was ensured by checking the temperature of the plates had cooled to ambient with a contact thermocouple at multiple points on each plate.

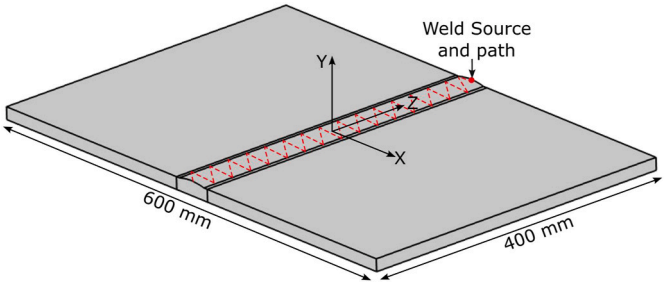

Fig. 2. Schematic of COMSOL domain for the final pass with co-ordinate system marking the centre of the domain.

For the thermal simulations, the welding source was modelled as a confined gaussian heat source [56,57] as defined in Eq. (4). Where φ_q is the heat flux in W/m^2, η is the weld efficiency factor, P is the weld power, r_{spot} is the arc radius, and r_{focus} is the spatially and temporally dependent centre of the gaussian function. A weld efficiency factor of 0.7 and spot size of 3 mm were used in this study. The weld power was determined by the multiplication of the voltage and the current for each pass as described in Table 1.

$$\varphi_q(x,z,t) = \frac{2\eta P}{\pi r_{spot}^2} e^{-\left(\frac{2r_{focus}^2}{r_{spot}^2}\right)}, t < t_{pass} \quad \text{Eq. 4}$$

$$r_{focus}(x,z,t) = \sqrt{\left(x - x_{focus}\right)^2 + \left(z - z_{focus}\right)^2} \quad \text{Eq. 5}$$

$$z_{focus}(t) = \left(a_z - \left(\frac{2a_z}{\pi}\cos^{-1}\left(\cos\left(\frac{2\pi}{p_z}t\right)\right)\right)\right), t < t_{pass} \quad \text{Eq. 6}$$

$$x_{focus}(t) = \frac{2A_x}{\pi}\sin^{-1}\left(sin\left(\frac{2\pi}{p_x}t\right)\right) + x_{offset}, t < t_{pass} \quad \text{Eq. 7}$$

With reference to the co-ordinate system in Fig. 2, Eqs. (5) and (6) mathematically describe the spatial and temporal variation in x_{focus} & z_{focus} which contribute to the vector sum of r_{focus}. x_{focus} is a triangular wave which describes the weaving pattern of the weld torch centre in the x-direction over time. The weave had an amplitude, A_x, and a period, p_x, that corresponded to the weld variables given in Table 1, while x_{offset} was adjusted to align with the centre of the next deposited weld pass – see Fig. 3(b). Likewise, z_{focus} is a triangular wave that describes the linear progression of the weld torch centre as the weld is progressed in the z-direction over time. The amplitude, A_z, corresponds to the maximum and minimum z position, and the period, p_z, was set to be double the pass time which is itself a function of linear velocity and weave frequency and alters for differing passes. x_{focus} & z_{focus} as they vary over time and space are shown in Fig. 2.

With all welding parameters defined, each model was run for double the time of a weld pass to observe how the thermal gradient changed over the domain during and after welding. Each model was solved in approximately 6 min and 48 s on a PC with a 3.8 GHz 24 core 3960X AMD thread ripper processor [58] and 128 Gb of RAM.

As both simulated and experimental data had been collected, it was possible to compare the two datasets. Temperature data from the simulated datasets were extracted at points corresponding to the placement of the thermocouples in the experiment and both the simulated and experimental data is shown in Fig. 5. With reference to Fig. 3, thermocouples were chosen to be plotted at various distances from the centre of the weld and at the top and the bottom of the plate in order to validate the observed thermal gradient at various points. Strong agreement between the experimental and simulated datasets is observed with an average error of 1.80% (mean error: 4.1 °C, max error: 19.2 °C). The variations from the simulation to what was observed were thought to be due to: 1) The positional error in mounting the thermocouples not exactly aligning with the exact points requested in the simulation; 2) the quality of the thermocouple attachment. The thermocouples are attached via spot welding and the quality of this bond influences the temperature reading; 3) Differences in the material properties; & 4) Differences in welding process parameters.

From the validation of the simulated data with the experimental data, the well-documented properties of S275 steel over temperature could be leveraged to create a spatially-varying material property map [32]. This spatial variation in material properties can be interpreted into a similar variation in ultrasonic velocity through the square root of the

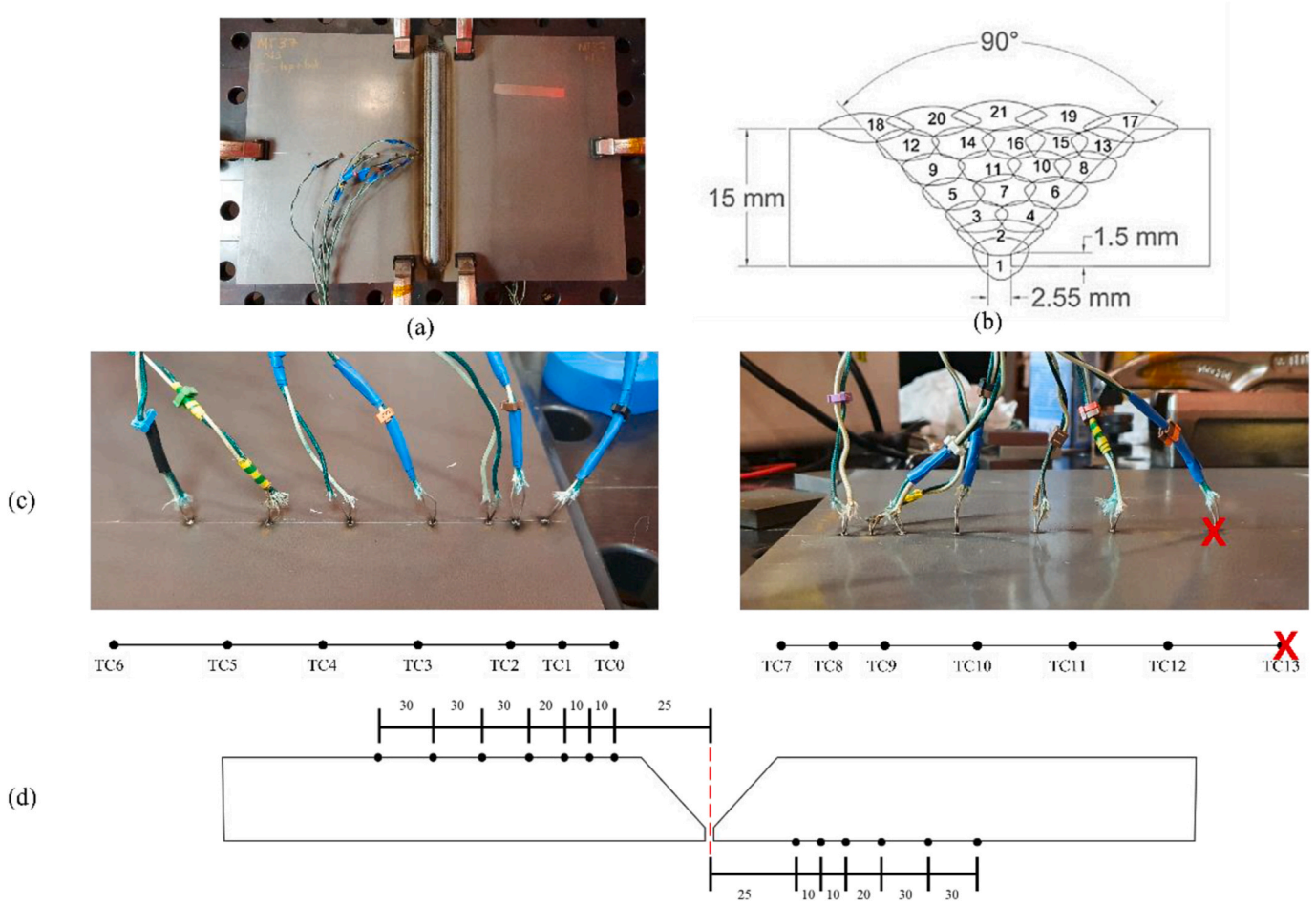

Fig. 3. Schematics describing the experimental setup. (a) A photograph showing the completed welded assembly of two 300 × 16 × 400 mm S275 carbon steel plates, (b) A cross-sectional schematic of the welded fabrication documenting the weld procedure specification where the numbers refer to the sequential order of each weld pass, (c) Photographs showing the experimental thermocouple placement along with their respective label where faulty thermocouples are denoted with a X (in red), (d) A schematic denoting the thermocouple placement with respect to the centre of the weld. Note: The distances shown are not to scale but occur in the same order as documented in Fig. 3(c). TC = Thermocouple. (For interpretation of the references to colour in this figure legend, the reader is referred to the Web version of this article.)

Table 1
Welding Parameters. * Automatic Voltage Correction (AVC) used in the robotically deployed weld process.

	AVC set voltage (V) *	Current (A)	Travel Speed (mm/min)	Wire Feed Speed (mm/min)	Weaving Amplitude (mm)	Weaving Frequency (Hz)
Pass 1	12	120	50	910	2	0.3
Pass 2	13.5	220	100	1225	4	0.6
Pass 3–16	13.5	210	120	1470	3	0.55
Pass 17–21	13.5	240	100	1225	4	0.6

materials stiffness divided by its density [59], and thus be used by any forward model to compute the necessary travel times as described in Section 2. It was thus hypothesised that these thermal models could be the *a priori* knowledge needed to accurately image ultrasonic datasets at the point of manufacture welded components.

4. Simulated thermal compensation

To prove the hypothesis that the validated thermal simulations could be used to accurately image high temperature welded components at the point of manufacture, several explicit FE proof-of-concept models producing FMC datasets were developed. These models were created and solved in the accelerated high-fidelity GPU-based FE package, Pogo, and were subsequently visualized using PogoPro [60].

The same standardised weld geometry used in Section 3 was modelled along with a 5 MHz COTS Olympus 5L32-A32 1D linear phased array [61] and an Olympus SA32C-ULT-N55SIHC ULTEM™ wedge [62] as shown in Fig. 7 (a). A 3 mm Side Drilled Hole (SDH) was modelled in the centre of the weld to assess the thermal compensation strategy. The mechanical properties for the ULTEM™ wedge were kept constant ($\rho = 1270\frac{kg}{m^3}, E = 2.89GPa, G = 1.04GPa$), whilst the steel material properties were allowed to vary with respect to temperature. It is important to note for an ultrasonic FE model in the presence of a thermal gradient, a spatially varying material property map needs to be created. This is done by leveraging the previously documented thermal gradient maps described in Section 3. Therefore, the temperature was interpolated from the nodal points of the mesh used in the FE model of the thermal environment to the nodal points of the mesh used in the ultrasonic FE model. Each unique temperature was modelled as a different material of the steel properties relating to their temperature as

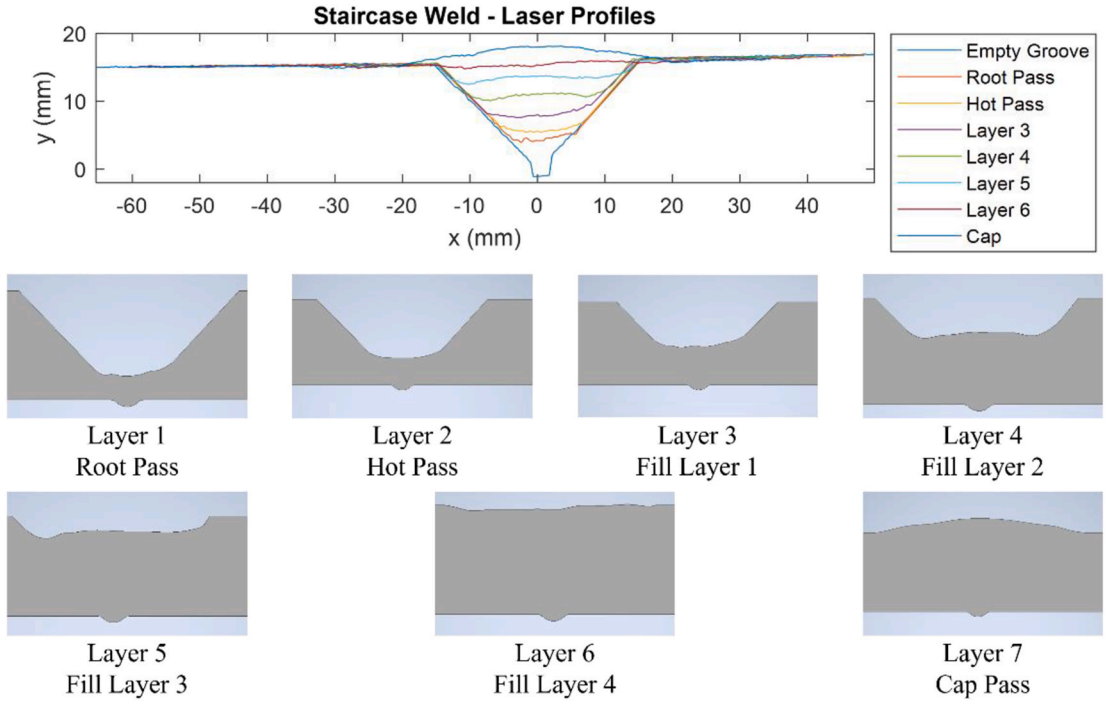

Fig. 4. Laser profiles of each layer along with 2D CAD schematics.

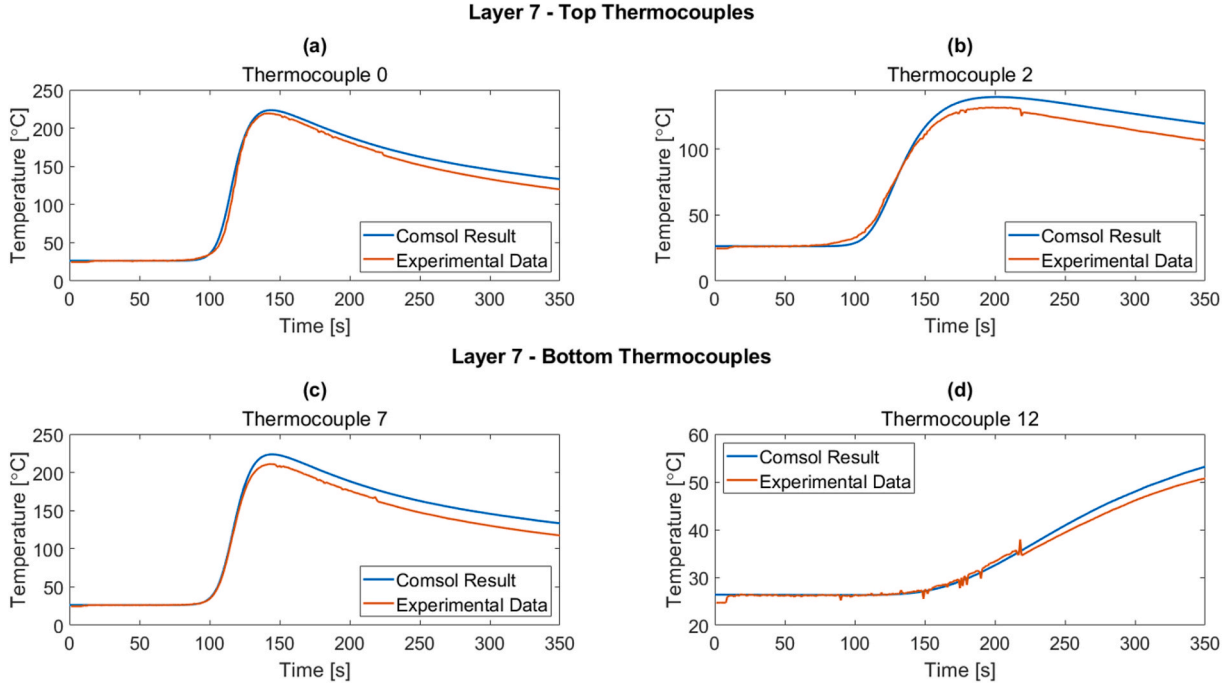

Fig. 5. Experimental and simulated thermal data comparison.

described in Fig. 6. To lower computational demands, a variable mesh was obtained via Pogo's internal mesher, pogoMesh, where the mesh element size was 1/16th of the slowest wavelength in each medium. This is illustrated in Fig. 7 (b). The full length of the welded plate was not modelled, and the domain was limited by Absorbing Layers with Increasing Dampening (ALID) [63] as shown in Fig. 9 (c). This effectively stopped any reflections from boundaries being seen in the imaging algorithm.

To aid development, each model was solved at 2 MHz initially, and when the modelling data had been validated, the frequency was increased to 5 MHz to match the centre frequency of the transducer itself. Each model was excited with a 2 MHz and 5 MHz 5 cycle Hann windowed toneburst respectively, and was solved with and without a thermal gradient being imposed on the steel domain creating a total of 4 models. The 2 MHz & 5 MHz models contained 18,069,054 & 117,729,711C3D6R elements respectively. It has been shown in literature that the C3D6R element can mesh complex geometries and simulate ultrasonic wave propagation problems effectively, hence it was used in this study [64–66]. The 2 MHz and 5 MHz models were solved in ~80 min and ~20hrs respectively on a HPC that contained two Nvidia

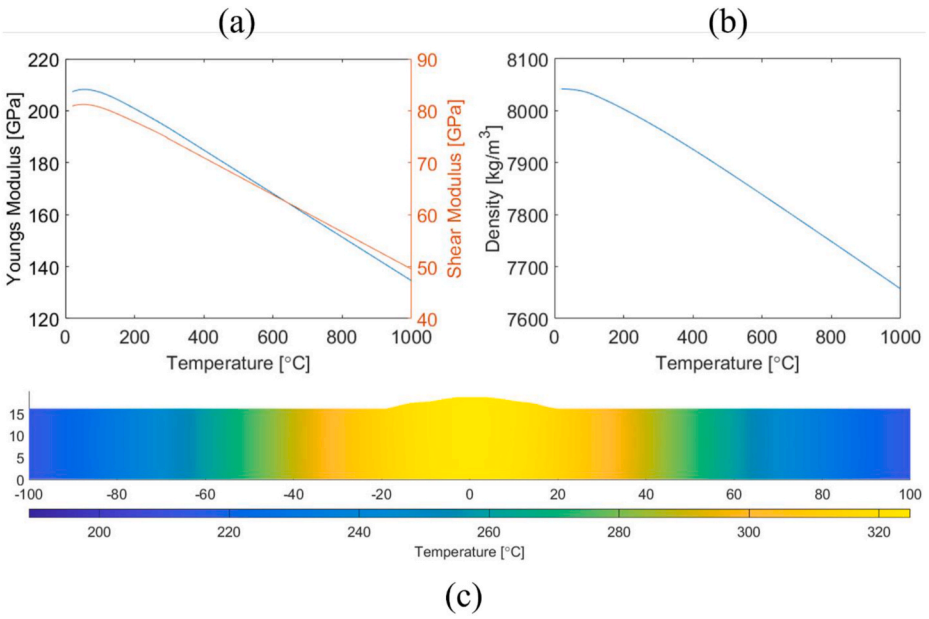

Fig. 6. S275 Material properties over temperature and thermal gradient from COMSOL simulation. (a) S275 Young's and Shear Modulus over temperature [32], (b) S275 Density over temperature [32], (c) Thermal gradient 100 mm behind the weld torch.

GeForce RTX 3090 graphics cards [67].

The resulting generated FMC datasets were imaged using the TFM algorithm in combination with the MSFMM as described in Section 2. For each frequency, three images were created: 1) An ambient image that used the room temperature (20 °C) FMC dataset and a room temperature ToF Map; 2) An uncompensated image that used a welded thermal gradient FMC dataset and a room temperature ToF map; and 3) A compensated image that used a welded thermal gradient FMC dataset and a welded thermal gradient ToF map.

Great effort was taken to ensure fast processing of the data. For each image, the MSFMM produced ToF maps using MATLABs parallel computing toolbox [68] in ~31 s on a HPC that housed two Intel Xeon Gold 6248R 48 core 3 GHz processors [69] with 192 Gb of RAM, while the TFM was performed in MATLABs GPU coder [70] in 1.6 s on the same HPC that housed two Nvidia GeForce RTX 3090 graphics cards [67]. Additionally, each image was formed on a spatial grid with a resolution of 20 pixels per millimetre. It has been shown in previously documented work [71] that for the frequencies and array used in this work, the Point Spread Function (PSF) of the array would limit the resolution to 0.08 mm, so the chosen value of 0.05 mm was well suited. The ToF calculation was bench marked against an Eikonal solver developed by the Consortium for Research in Elastic Wave Exploration Seismology (CREWES) [72] at the University of Calgary and provided accurate ToF maps in ~4 h. This result demonstrates the benefits of using the MSFMM due its inherently fast solve times no noticeable image degradation as documented in Section 1.

The results for the 2 MHz and 5 MHz models are shown in Figs. 8 and 9 respectively where each image derived from each transversal half skip is displayed above each other [73]. The SNR was very similar across all three images for both the 2 MHz & 5 MHz datasets, as documented in Table 2. This implies that the thermal gradient has little defocusing effect. However, the accuracy of the reflector's position is significantly improved when thermal compensation is incorporated. To quantify this improvement, the position of the maximum amplitude was recorded and compared across all the three images for both the 2 MHz and 5 MHz datasets. It was shown that by not compensating for the thermal effects associated with a typical welding process, a maximum positional error of 4.34 mm & 3.81 mm was introduced for the 2 MHz and 5 MHz datasets respectively – see the images in Fig. 8 (b) & Fig. 9 (b). By compensating, the maximum error in the reflector's position was reduced to maximum of 0.2 mm & 0.46 mm for the 2 MHz and 5 MHz datasets respectively representing a $\geq$ 85% decrease in positional error across all images – see the images in Fig. 8 (c) & Fig. 9 (c). These results are summarised in Table 2. It is thought that the larger error observed in the 5 MHz dataset was due to the lower wavelength and greater resolving capacity inherently associated with higher frequency datasets.

This result is further emphasised in the averaged ToF maps from every transmit receive pair 15 mm either side of the reflector as shown in Fig. 10. Between the high temperature and ambient ToF maps documented Fig. 10 (a) and (b) respectively, a difference of 1.34 μs is reported at the reflector location. It is noted that these times represent the time taken for the wavefront to travel from transducer to the imaging domain, and to calculate the full travel time back to the transducer this value would need to be doubled. This represents a 4 mm positional shift for an assumed constant transverse ultrasonic velocity of 3000 m/s. A 4 mm positional shift in the reflector location estimated in this manner is of the same order of magnitude observed in Table 2. Furthermore, the ToF map illustrated in Fig. 10 (a) shows the correct reflector contour pulling the defect position towards the left of the imaging domain. This is expected and counteracts the shift to the right documented in the uncompensated images in Fig. 8 (b) and Fig. 9 (b). Therefore, by comparing ToF maps in this manner, an approximate positional shift magnitude and direction can be estimated.

These results confirm that for a simulated noise-free environment, the proposed thermal compensation strategy has a positive effect on imaging performance. To confirm these results and trends hold true in a realistic setting at the point of manufacture, several experiments were conducted.

5. Experimental thermal compensation

5.1. Initial experimental results

To further prove our hypothesis that the validated thermal simulations could be used to accurately image welded components at the point of manufacture with thermal gradients present, several experiments were conducted. A 15.8 mm thick carbon steel sample with two 2 mm SDHs machined along the weld groove interface at one third and two thirds the thickness to act as reflectors, was procured for an autogenous weld to be applied. Here, an autogenous weld refers to the application of

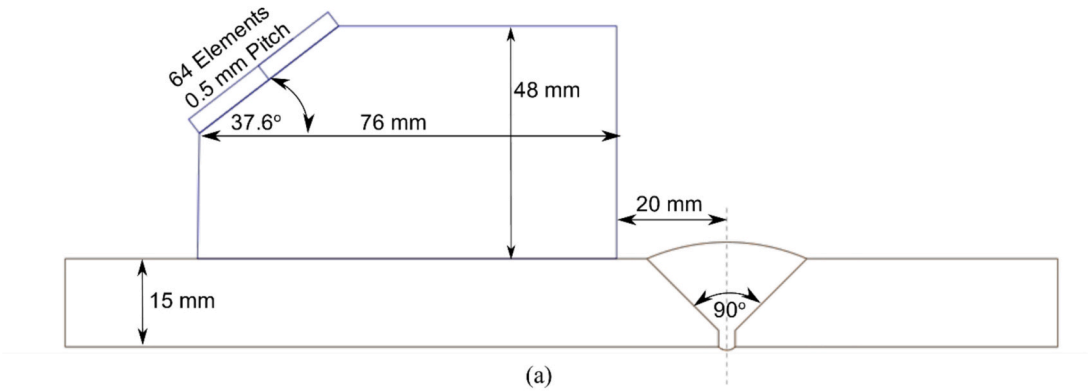

(a)

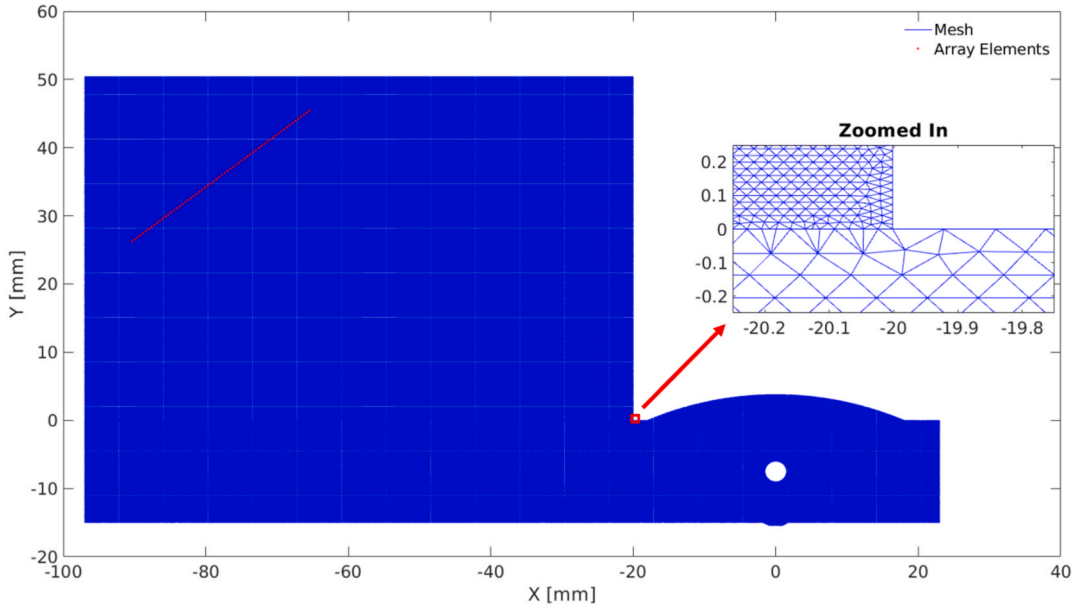

(b)

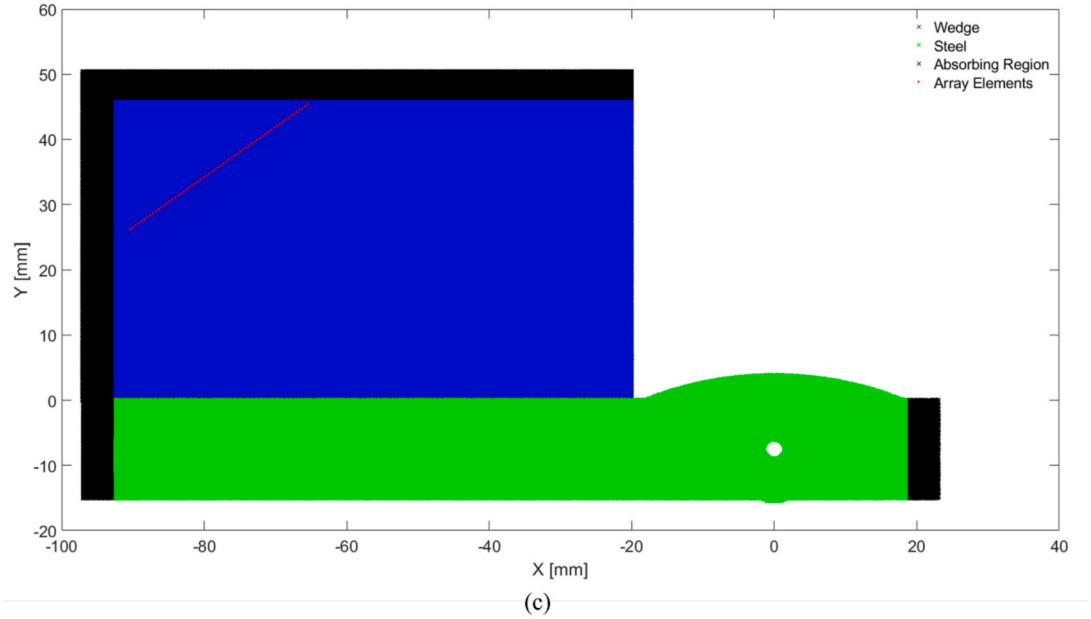

(c)

Fig. 7. Schematics of proof-of-concept FE models (a) Overall geometric domain, size, and positioning, (b) Variable mesh size created in pogoMesh, (c) Overall FE domain showing the wedge, steel, and absorbing regions as well as the 3 mm SDH and array element positions.

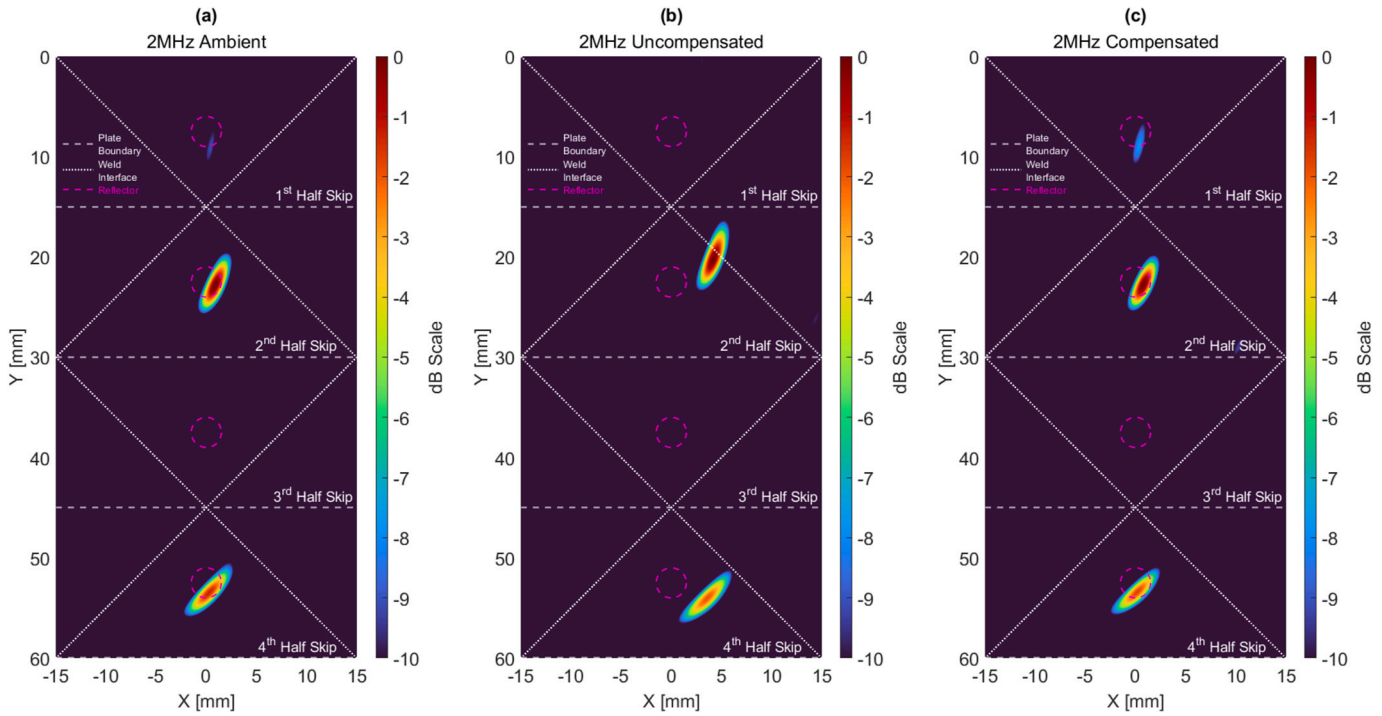

Fig. 8. TFM images formed with ToF maps from the MSFMM. (a) TFM image constructed with FMC data simulated at 2 MHz ambient room temperature material properties and an ambient room temperature ToF map, (b) TFM image constructed with FMC data simulated at 2 MHz with thermally varying material properties over the steel domain and an ambient room temperature ToF map, & (c) TFM image constructed with FMC data simulated at 2 MHz with thermally varying material properties and ToF map over the steel domain.

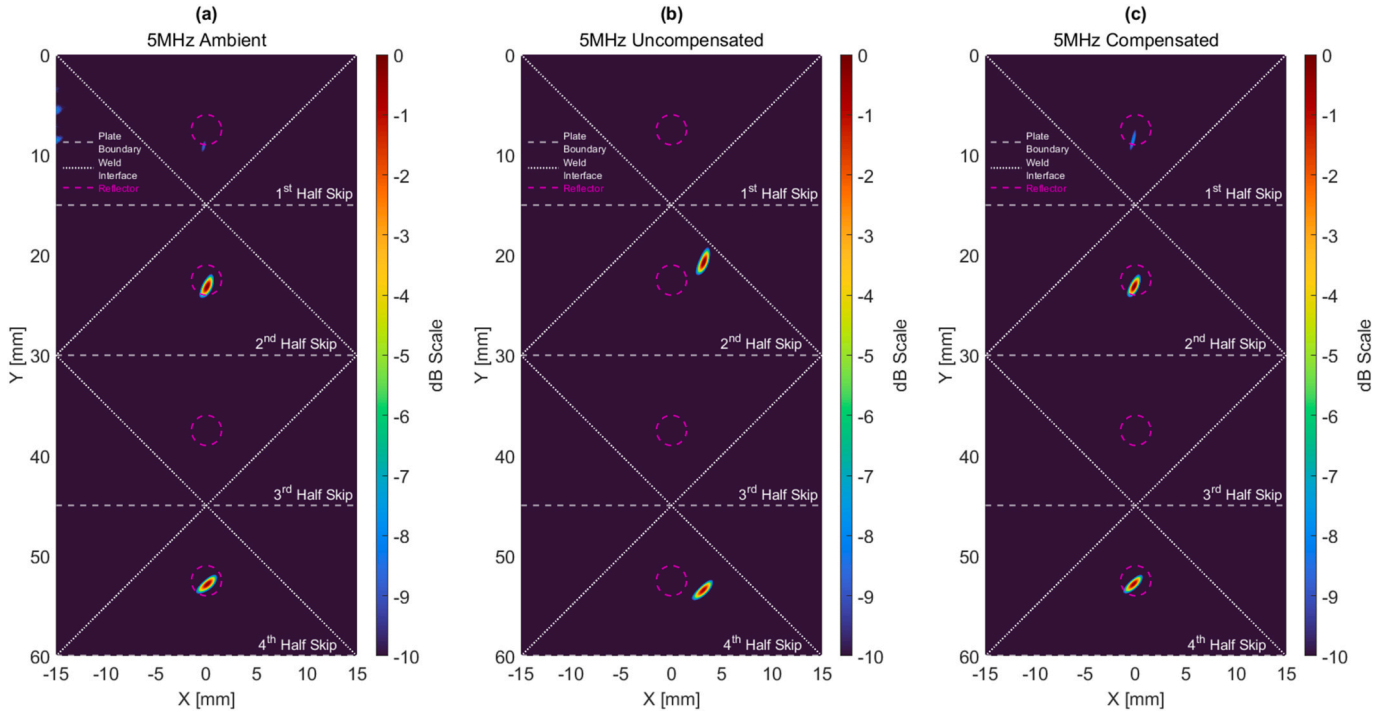

Fig. 9. TFM images formed with ToF maps from the MSFMM. (a) TFM image constructed with FMC data simulated at 5 MHz ambient room temperature material properties and an ambient room temperature ToF map, (b) TFM image constructed with FMC data simulated at 5 MHz with thermally varying material properties over the steel domain and an ambient room temperature ToF map, & (c) TFM image constructed with FMC data simulated at 5 MHz with thermally varying material properties and ToF map over the steel domain.

a TIG welding heat source on the surface of the plate without the addition of any filler material. The position of these reflectors was selected to mimic lack of sidewall fusion defects. The acquisition set up involved the use of two robots. A KUKA Quantec Extra HA KR-90 R3100 [74] was used to perform the welding sequence and a Kuka KR6 R900 Agilus [75] in combination with a IP-65 rated gamma force-torque

Table 2
Imaging performance summary for the simulated datasets stating the positional error and SNR observed in the TFM images.

	Reflector in 2nd Half Skip		Reflector in 4th Half Skip	
	SNR (dB)	Location Shift (mm)	SNR (dB)	Location Shift (mm)
2 MHz – Room Temp	23.3	0	21.7	0
2 MHz – High Temp – Uncompensated	23.5	4.34	22.0	3.81
2 MHz – High Temp – Compensated	24.0	0.2	22.6	0.32
5 MHz – Room temp	27.1	0	33.5	0
5 MHz – High Temp – Uncompensated	27.0	3.44	33.5	3.06
5 MHz – High Temp – Compensated	25.9	0.11	34.3	0.46

sensor from ATI Industrial Automation [76] was used to record the ultrasonic data. Both robots were controlled via a KRC 4 controller [77] using the Kuka Robot Sensor Interface (RSI) [78]. The force torque sensor was used to apply a force of 120 N in the Z-direction during the ultrasonic data acquisition to ensure consistent coupling. High temperature couplant [79] was applied between the transducer and wedge as well as between the wedge and sample. The FMC data was captured using a PEAK NDT LTPA 64 + 64 phased array controller [80] from an Olympus 5 MHz 5L32-A32 1D linear phased array and an Olympus SA32C-ULT-N55SIHC ULTEM™ wedge along with a 6 mm thick polymer coupling medium. To reduce the presence of artefacts, all experimental FMC datasets were filtered around the centre frequency of the transducer in the model using a Hann window with a bandwidth of 60% of the centre frequency. The experimental setup is illustrated in Fig. 11.

Initially, an FMC dataset was acquired and imaged at room temperature prior to the application of the autogenous weld for simplicity and comparison. The acquired room temperature data was imaged using the same code as in Section 4 and is shown in Fig. 12 where each image derived from each transversal half skip is displayed above each other [73].

With datasets acquired and successfully imaged under ambient conditions, the autogenous weld was then applied. As the autogenous weld was laid, a thermal gradient was induced into the steel and was again logged via K-type thermocouples as in Section 3. The original COMSOL thermal models were altered slightly to account for the use of an autogenous weld in the experimental procedure and strong agreement (mean error: 4.6 °C, max error: 8.6 °C) was again observed between the thermally simulated and experimentally recorded thermal datasets. As the acquisition of thermal and ultrasonic datasets was performed in a semi-autonomous fashion, each dataset could be matched with ease by analysing their timestamp. FMC datasets were acquired after the maximum temperature recorded by the thermocouples was less than 150 °C. This conservative criterion was used to avoid hardware failure as the ULTEM™ wedge has an operating temperature of ~150 °C as recommended by the wedge manufacturer. Beamformed images were displayed in real time at the point of acquisition showed that the coupling had stabilised. An FMC dataset with stable coupling was then elected for compensation, and a thermal gradient corresponding to this was selected from the COMSOL model and is shown in Fig. 13. In this part of the work, the silicone coupling medium and ULTEM™ wedge were not modelled in the thermal simulations, and as a result they have an assumed ambient temperature of 20 °C across their entire domains.

The uncompensated and steel gradient-compensated TFM images produced from the FMC data and initial thermal gradient are shown in Fig. 14 (a) and (b) respectively, where each image derived from each transversal half skip is displayed above each other [73]. A SNR of 18.6 dB was reported for Reflector 2 in the uncompensated high-temperature image, and a very similar SNR of 16.7 dB was reported for Reflector 2 in the steel gradient-compensated high-temperature TFM images. This agrees with the trend observed in the simulated data where comparable

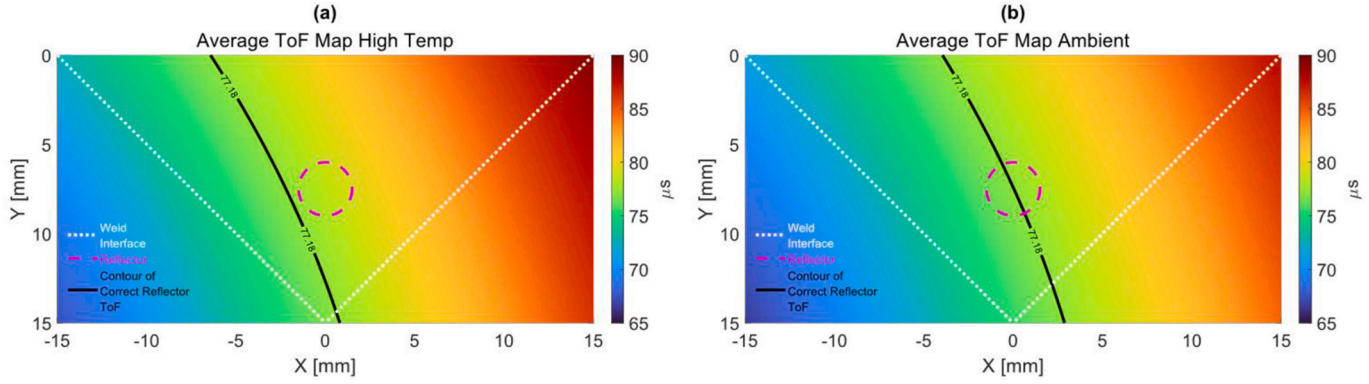

Fig. 10. Zoomed in ToF maps, (a) 5 MHz ambient ToF map 15 mm either side of the reflector. (b) 5 MHz high temp ToF map 15 mm either side of the reflector.

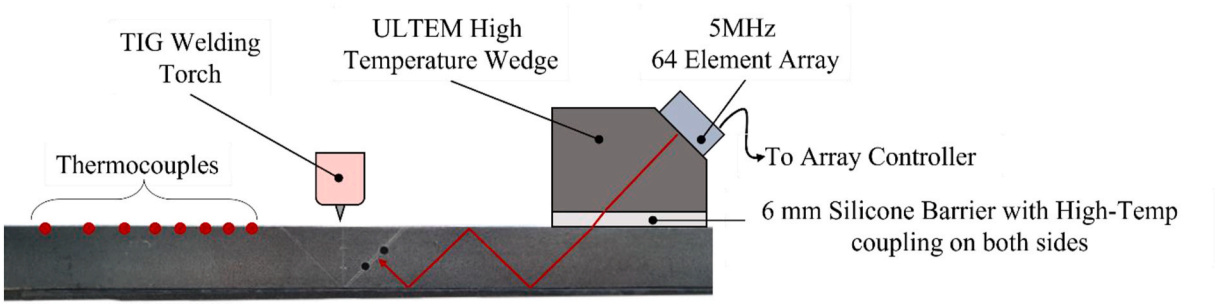

Fig. 11. Experimental setup depicting the approximate location of the thermocouples, weld torch, polymer coupling medium, ultrasonic wedge, and array on top of the carbon steel component.

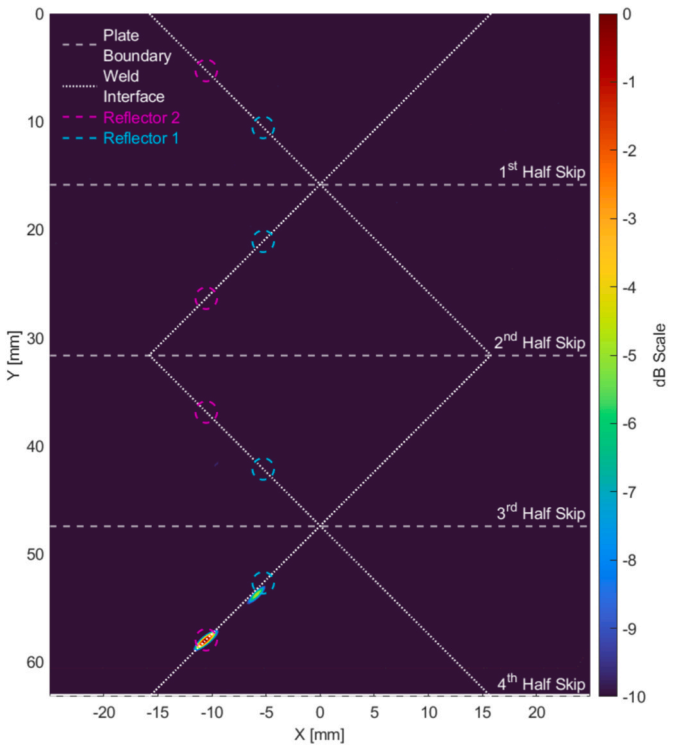

Fig. 12. Experimental ambient temperature TFM image created with ToF maps from the MSFMM.

SNRs are reported for uncompensated and compensated images. Like the simulated datasets, a positive benefit was observed when the uncompensated and steel gradient-compensated reflector positions were compared. A 20.5% reduction in positional error was reported between the uncompensated and steel gradient-compensated high-temperature images, with an absolute positional error of 4.49 mm and 3.57 mm for Reflector 2 respectively.

5.2. Incorporating coupling & wedge thermal gradients

While the initial experimental results at the point of manufacture demonstrated an improvement in the position of the reflector, these did not incorporate thermal gradients within the wedge and coupling medium.

A further series of experiments were performed to understand how the ultrasonic velocity varied within the polymer coupling medium and ULTEM™ wedge with temperature. Experimental pulse-echo time of flight measurements, across known depth samples of each material were undertaken across the working temperature range. The COMSOL models were then updated to incorporate the thermal gradient in the wedge and coupling medium. Isothermal boundary conditions were applied at the steel-silicone and silicone- ULTEM™ interfaces, while ambient convection and radiation boundary conditions of 20 °C were applied at all air interfaces. The ULTEM™ wedge and silicone polymer coupling medium were modelled with a specific heat capacity of 2000 $\frac{J}{kgK}$ & 1430.15 $\frac{J}{kgK}$ and thermal conductivity of 0.22 $\frac{W}{mK}$ & 0.143 $\frac{W}{mK}$, respectively. The updated thermal gradient is shown in Fig. 15 with an average predicted temperature in the polymer coupling medium and wedge of 29.15 °C and 20 °C, respectively.

The updated thermal gradient was used to produce a new ToF map through the MSFMM and the TFM images were reconstructed once more. The updated TFM image is shown in Fig. 16 (d) along with comparisons to images formed with: 1) ambient FMC data and an ambient thermal gradient (Fig. 16 (a)); 2) high temperature FMC data and an ambient thermal gradient (Fig. 16 (b)); 3) high temperature FMC data corrected with a thermal gradient only in the steel domain (Fig. 16 (c)). The imaging performance is summarised in Table 3. It is again noted that the updated image in Fig. 16 (d) produced a comparable SNR to the other images formed from the same FMC dataset in line with previous results documented in this study. A positive increase in positional accuracy is also observed, with the reflector position error decreasing by a further 53% from the initial steel-compensation attempt – see Fig. 14 (b)/Fig. 16 (c) – to an absolute error of 1.68 mm. It is thought that the remaining 1.68 mm positional error can be attributed to errors in the thermal gradient, errors in our understanding of how the ultrasonic velocity varies over temperature, and positional inaccuracies between the modelling domains and reality. When the updated thermal compensation strategy is compared to the uncompensated case, an approximate 3 mm reduction in absolute positional error is observed, proving the efficacy of using this strategy to inspect at the point of manufacture in the presence of high-temperature gradients, and aiding industry as it moves towards higher throughput production lines associated with Industry 4.0.

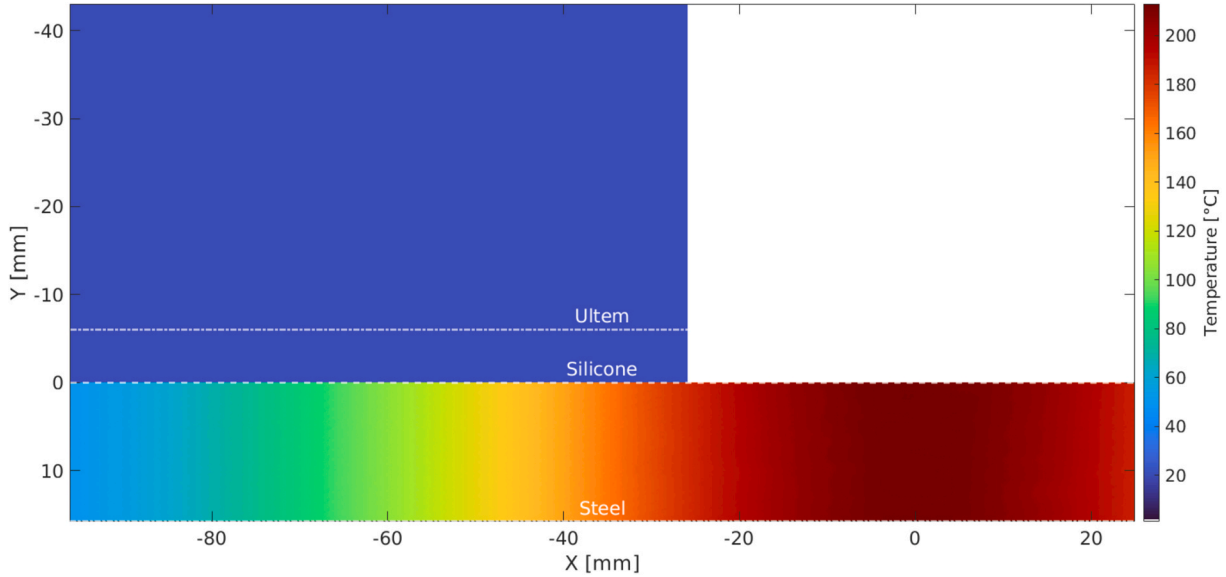

Fig. 13. Extrapolated 2D thermal gradient from the COMSOL model that mimicked the experimental autogenous weld procedure.

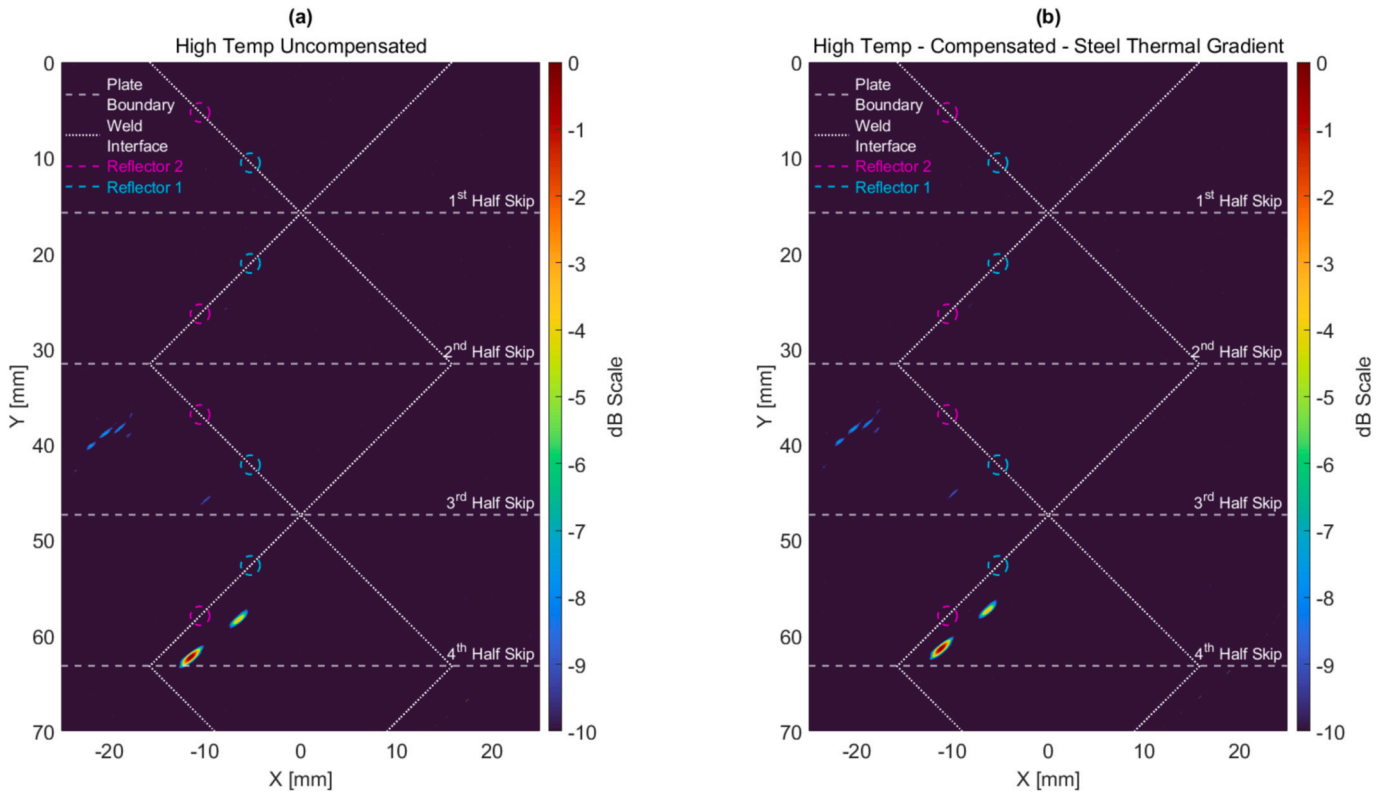

Fig. 14. Experimental high temperature TFM Images created with ToF maps from the MSFMM (a) Uncompensated TFM image showing a positional error with respect to Reflector 2 of 4.49 mm, & (b) Thermally compensated TFM image using a thermal gradient only in the steel plate showing a positional error with respect to Reflector 2 of 3.57 mm.

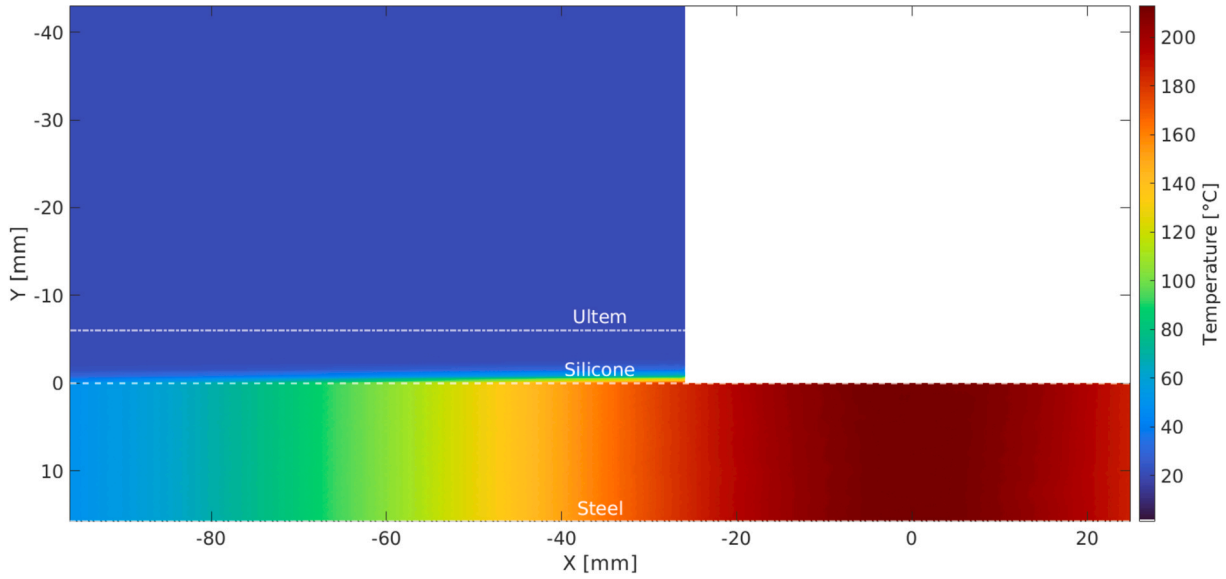

Fig. 15. Updated thermal gradient in the steel, silicone polymer coupling medium and ULTEM™ wedge.

6. Concluding remarks

Traditionally, ultrasonic inspection of welded components has been performed after the component has been manufactured due to industrial protocol and the technical challenges associated with inspecting at the point of manufacture. As businesses seek continual process improvements as they move towards Industry 4.0, the time lost due to this practice is now undesirable and there is a desire to move inspection to the point of manufacture. Technically, inspecting welded components at the point manufacture is challenging due to the elevated temperature and resulting thermal gradients in the component introducing beam bending effects due to refraction and positional inaccuracies in the ultrasonic data. In this paper we present, for the first time, generalised time of flight maps to be created via the Multi-Stencils Fast Marching Method (MSFMM), incorporating thermal gradient information from the welding process and compensating for positional inaccuracy in defect

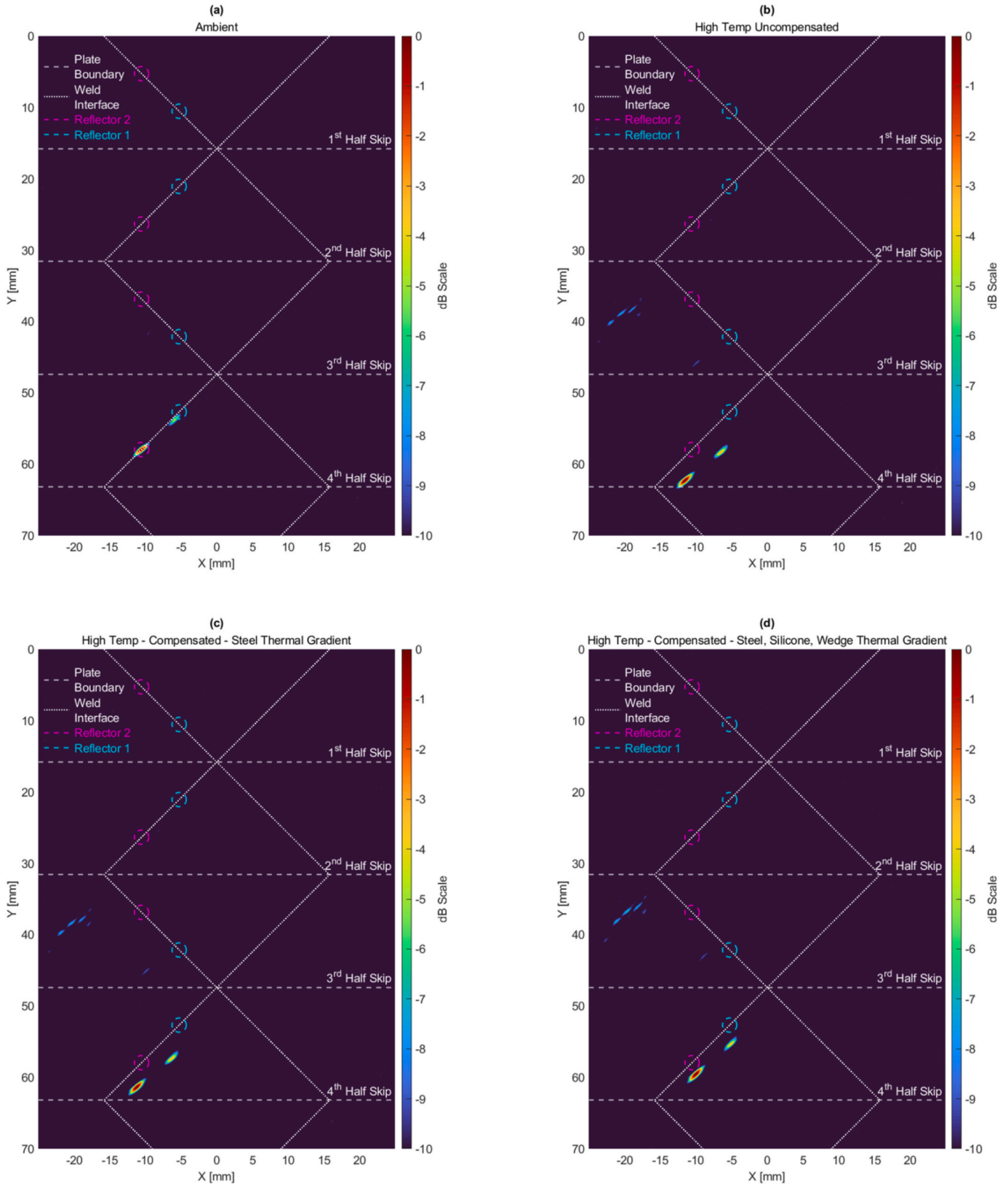

Fig. 16. Experimental TFM images created with ToF maps from the MSFMM (a) TFM image of ambient FMC data, (b) Uncompensated TFM image of high temperature FMC data showing a positional error with respect to Reflector 2 of 4.49 mm, (c) Thermally compensated TFM image of high temperature FMC data using a thermal gradient only in the steel plate showing a positional error with respect to Reflector 2 of 3.57 mm, & (d) Thermally compensated TFM image of high temperature FMC data using a thermal gradient only in the steel, silicone, and ULTEM™ domains showing a positional error with respect to Reflector 2 of 1.68 mm.

Table 3
Imaging performance summary for the experimental datasets stating the positional error and SNR observed for Reflector 2 in the 4th half skip of the TFM images.

Dataset	SNR (dB) of Reflector 2	Location Shift (mm) of Reflector 2
Ambient	18.6	0
High Temp - Uncompensated	16.7	4.49
High Temp - Steel Gradient - Compensated	16.5	3.57
High Temp - Full Domain-Gradient-Compensated	16.4	1.68

location in resultant TFM images.

To document the thermal gradients experienced during a standard TIG welding procedure, various 3-dimensional thermal simulations were developed and experimentally validated with an average error of 1.80% (mean error: 4.1°C, max error: 19.2°C). The resulting thermal information of the welding domain along with well-defined material properties that varied over temperature allowed for the generation of generic ToF maps through the MSFMM method, and the ultrasonic data to be imaged by the TFM. The proposed thermal compensation strategy was initially evaluated on synthetically generated finite element data and showed an improvement in positional accuracy of reflectors of at ~3 mm. Experimental results also showed a similar trend with a ~3 mm improvement in reflector positional accuracy. Out of reflector detection, focusing performance, and positional accuracy, it can be said that an improvement in the latter can be observed from the proposed thermal compensation strategy which is crucial for in-process weld inspection. The results show how high-quality ultrasonic images can be generated in process and demonstrate a significant step closer to inspection at the point of manufacture.

While the proposed thermal compensation scheme introduces additional upfront requirements over traditional phased array inspection, such as in-depth understanding of the welding process and resulting thermal gradients, as well as in-depth material property characterisation namely the material stiffness and density over temperature, it is believed that it offers the most benefit for mass manufactured and high-quality welded components.

In future work, the authors plan to investigate real-time in-process thermally compensated imaging using the MSFMM, extend the technique to austenitic materials and welds of complex geometry, as well as explore and quantify the effect of thermal gradient distribution and magnitude has on reflector positioning and focusing.

Author statement

Euan Foster: Data curation, Original draft preparation, Reviewing and editing, Software, Formal Analysis, Investigation.

Charles MacLeod: Supervision, Reviewing and editing, Conceptualization, Methodology.

Ehsan Mohseni: Supervision, Reviewing and editing, Investigation.

Anthony Gachagan: Supervision, Reviewing and editing.

Gareth Pierce: Supervision, Reviewing and editing.

Katherine Tant: Software, Supervision, Reviewing and editing, Conceptualization, Methodology.

Muhammad K. Rizwan: Supervision, Reviewing and editing, Investigation.

Ewan Nicolson: Software, Formal Analysis, Investigation, Reviewing and editing, Validation.

Nina E. Sweeney: Reviewing and editing, Software, Formal Analysis, Investigation, Validation.

David Lines: Supervision, Reviewing and editing, Software, Formal Analysis, Investigation.

Jonathan Singh: Reviewing and editing, Software, Formal Analysis, Investigation.

Declaration of competing interest

The authors declare that they have no known competing financial interests or personal relationships that could have appeared to influence the work reported in this paper.

Data availability

Data will be made available on request.

Acknowledgements

This work is supported by the UK Research Centre for Non-Destructive Evaluation (RCNDE) 4 Core Research Program.

We would like to thank Dr. Peter Huthwaite of Imperial College London and James Ludlam from the University of Strathclyde for their help and useful discussions.

References

[1] Drinkwater BW, Wilcox PD. Ultrasonic arrays for non-destructive evaluation: a review. NDT E Int 2006;39:525–41. https://doi.org/10.1016/j.ndteint.2006.03.006.

[2] Krautkrämer J, Krautkrämer H. Ultrasonic testing of materials. Springer Science & Business Media; 2013.

[3] Fan C, Caleap M, Pan M, Drinkwater BW. A comparison between ultrasonic array beamforming and super resolution imaging algorithms for non-destructive evaluation. Ultrasonics 2014;54:1842–50. https://doi.org/10.1016/j.ultras.2013.12.012.

[4] Le Jeune L, Robert S, Lopez Villaverde E, Prada C. Plane Wave Imaging for ultrasonic non-destructive testing: generalization to multimodal imaging. Ultrasonics 2016;64:128–38. https://doi.org/10.1016/j.ultras.2015.08.008.

[5] Holmes C, Drinkwater BW, Wilcox PD. Post-processing of the full matrix of ultrasonic transmit–receive array data for non-destructive evaluation. NDT E Int 2005;38:701–11. https://doi.org/10.1016/j.ndteint.2005.04.002.

[6] Camacho J, Parrilla M, Fritsch C. Phase coherence imaging. IEEE Trans Ultrason Ferroelectrics Freq Control 2009;56:958–74. https://doi.org/10.1109/TUFFC.2009.1128.

[7] Hunter AJ, Drinkwater BW, Wilcox PD. The wavenumber algorithm for full-matrix imaging using an ultrasonic array. IEEE Trans Ultrason Ferroelectrics Freq Control 2008;55:2450–62. https://doi.org/10.1109/TUFFC.952.

[8] Portzgen N, Gisolf D, Blacquiere G. Inverse wave field extrapolation: a different NDI approach to imaging defects. IEEE Trans Ultrason Ferroelectrics Freq Control 2007;54:118–27. https://doi.org/10.1109/TUFFC.2007.217.

[9] Zhang J, Drinkwater BW, Wilcox PD, Hunter AJ. Defect detection using ultrasonic arrays: the multi-mode total focusing method. NDT E Int 2010;43:123–33. https://doi.org/10.1016/j.ndteint.2009.10.001.

[10] Wilcox PD, Croxford AJ, Budyn N, Bevan RLT, Zhang J, Kashubin A, et al. Fusion of multi-view ultrasonic data for increased detection performance in non-destructive evaluation. Proc R Soc Math Phys Sci 2020;476. https://doi.org/10.1098/rspa.2020.0086.

[11] Bevan RLT, Budyn N, Zhang J, Croxford AJ, Kitazawa S, Wilcox PD. Data fusion of multiview ultrasonic imaging for characterization of large defects. IEEE Trans Ultrason Ferroelectrics Freq Control 2020;67:2387–401. https://doi.org/10.1109/TUFFC.2020.3004982.

[12] Budyn NS, Croxford AJ, Bevan RLT, Zhang J, Wilcox PD. Characterisation of small embedded two-dimensional defects using multi-view Total Focusing Method imaging algorithm. NDT E Int 2021;119. https://doi.org/10.1016/j.ndteint.2021.102413.

[13] Stratoudaki T, Clark M, Wilcox P. Adapting the full matrix capture and the Total Focusing Method to laser ultrasonics for remote non destructive testing. In: 2017 IEEE international ultrasonics symposium, IUS 2017. 2017 IEEE int ultrason symp IUS 2017; 2017. https://doi.org/10.1109/ULTSYM.2017.8092900.

[14] Stratoudaki T, Clark M, Wilcox PD. Full matrix capture and the total focusing imaging algorithm using laser induced ultrasonic phased arrays. AIP Conf Proc 2017;1806:020022. https://doi.org/10.1063/1.4974563.

[15] Stratoudaki T, Clark M, Wilcox PD. Laser induced ultrasonic phased array using full matrix capture data acquisition and total focusing method. Opt Express 2016;24:21921–38. https://doi.org/10.1364/OE.24.021921.

[16] Mineo C, Lines D, Cerniglia D. Generalised bisection method for optimum ultrasonic ray tracing and focusing in multi-layered structures. Ultrasonics 2021;111:106330. https://doi.org/10.1016/j.ultras.2020.106330.

[17] Mineo C, Cerniglia D, Mohseni E. Solving ultrasonic ray tracing in parts with multiple material layers through Root-Finding methods. Ultrasonics 2022;124:106747. https://doi.org/10.1016/j.ultras.2022.106747.

[18] Nowers O, Duxbury DJ, Drinkwater BW. Ultrasonic array imaging through an anisotropic austenitic steel weld using an efficient ray-tracing algorithm. NDT E Int 2016;79:98–108. https://doi.org/10.1016/j.ndteint.2015.12.009.

[19] Connolly GD, Lowe MJS, Temple JaG, Rokhlin SI. Correction of ultrasonic array images to improve reflector sizing and location in inhomogeneous materials using

a ray-tracing model. J Acoust Soc Am 2010;127:2802–12. https://doi.org/10.1121/1.3372724.
[20] Nowers O, Duxbury DJ, Zhang J, Drinkwater BW. Novel ray-tracing algorithms in NDE: application of Dijkstra and A* algorithms to the inspection of an anisotropic weld. NDT E Int 2014;61:58–66. https://doi.org/10.1016/j.ndteint.2013.08.002.
[21] Tant KMM, Galetti E, Mulholland AJ, Curtis A, Gachagan A. A transdimensional Bayesian approach to ultrasonic travel-time tomography for non-destructive testing. Inverse Probl 2018;34:095002. https://doi.org/10.1088/1361-6420/aaca8f.
[22] Tant KMM, Galetti E, Mulholland AJ, Curtis A, Gachagan A. Effective grain orientation mapping of complex and locally anisotropic media for improved imaging in ultrasonic non-destructive testing. Inverse Probl Sci Eng 2020;28:1694–718. https://doi.org/10.1080/17415977.2020.1762596.
[23] Javadi Y, Vasilev M, MacLeod CN, Pierce SG, Su R, Mineo C, et al. Intentional weld defect process: from manufacturing by robotic welding machine to inspection using TFM phased array. AIP Conf Proc 2019;2102:040011. https://doi.org/10.1063/1.5099761.
[24] Zimermann R, Mohseni E, Lines D, Vithanage RKW, MacLeod CN, Pierce SG, et al. Multi-layer ultrasonic imaging of as-built Wire + Arc additive manufactured components. Addit Manuf 2021;48. https://doi.org/10.1016/j.addma.2021.102398.
[25] Vithanage RKW, Mohseni E, Lines D, Loukas C, Foster E, MacLeod CN, et al. Development of a phased array ultrasound roller probe for inspection of wire + arc additive manufactured components. J Manuf Process 2022;80:765–74. https://doi.org/10.1016/j.jmapro.2022.06.045.
[26] Zimermann R, Mohseni E, Vasilev M, Loukas C, Vithanage RKW, Macleod CN, et al. Collaborative robotic wire + Arc Additive manufacture and sensor-enabled in-process ultrasonic non-destructive evaluation. Sensors 2022;22:4203. https://doi.org/10.3390/s22114203.
[27] Möhring RH, Schilling H, Schütz B, Wagner D, Willhalm T. Partitioning graphs to speed up dijkstra's algorithm. In: Nikoletseas SE, editor. Exp. Effic. Algorithms. Berlin, Heidelberg: Springer; 2005. p. 189–202. https://doi.org/10.1007/11427186_18.
[28] Crauser A, Mehlhorn K, Meyer U, Sanders P. A parallelization of Dijkstra's shortest path algorithm. In: Brim L, Gruska J, Zlatuška J, editors. Math. Found. Comput. Sci. 1998. Berlin, Heidelberg: Springer; 1998. p. 722–31. https://doi.org/10.1007/BFb0055823.
[29] Huang B, Wu Q, Zhan FB. A shortest path algorithm with novel heuristics for dynamic transportation networks. Int J Geogr Inf Sci 2007;21:625–44. https://doi.org/10.1080/13658810601079759.
[30] Bourne DP, Mulholland AJ, Sahu S, Tant KMM. An inverse problem for Voronoi diagrams: A simplified model of non-destructive testing with ultrasonic arrays. Math Methods Appl Sci 2021;44:3727–45. https://doi.org/10.1002/mma.6977.
[31] Singh J, Tant K, Curtis A, Mulholland A. Real-time super-resolution mapping of locally anisotropic grain orientations for ultrasonic non-destructive evaluation of crystalline material. Neural Comput Appl 2022;34:4993–5010. https://doi.org/10.1007/s00521-021-06670-8.
[32] Scruby CB, Moss BC. Non-contact ultrasonic measurements on steel at elevated temperatures. NDT E Int 1993;26:177–88. https://doi.org/10.1016/0963-8695(93)90472-7.
[33] Silber FA, Ganglbauer C. Ultrasonic testing of hot welds. Non-Destr Test 1970;3:429–32. https://doi.org/10.1016/0029-1021(70)90156-8.
[34] Javadi Y, Mohseni E, MacLeod CN, Lines D, Vasilev M, Mineo C, et al. Continuous monitoring of an intentionally-manufactured crack using an automated welding and in-process inspection system. Mater Des 2020;191. https://doi.org/10.1016/j.matdes.2020.108655.
[35] Lines D, Javadi Y, Mohseni E, Vasilev M, MacLeod CN, Mineo C, et al. A flexible robotic cell for in-process inspection of multi-pass welds. Insight J Br Inst Non-Destr Test 2020;62:526–32. https://doi.org/10.1784/insi.2020.62.9.526.
[36] Javadi Y, Mohseni E, MacLeod CN, Lines D, Vasilev M, Mineo C, et al. High-temperature in-process inspection followed by 96-h robotic inspection of intentionally manufactured hydrogen crack in multi-pass robotic welding. Int J Pres Ves Pip 2021;189. https://doi.org/10.1016/j.ijpvp.2020.104288.
[37] Vithanage RKW, Mohseni E, Qiu Z, MacLeod C, Javadi Y, Sweeney N, et al. A phased array ultrasound roller probe for automated in-process/interpass inspection of multipass welds. IEEE Trans Ind Electron 2021;68:12781–90. https://doi.org/10.1109/TIE.2020.3042112.
[38] ISO 13588:2019 - Non-destructive testing of welds — ultrasonic testing — use of automated phased array technology. Int Stand Organ n.d.
[39] ISO 17640:2018 - Non-destructive testing of welds — ultrasonic testing — techniques, testing levels, and assessment. Int Stand Organ n.d.
[40] ISO 19285:2017- Non-destructive testing of welds — phased array ultrasonic testing (PAUT) — acceptance levels. Int Stand Organ n.d.
[41] Wang Z. An imaging and measurement system for robust reconstruction of weld pool during arc welding. IEEE Trans Ind Electron 2015;62:5109–18. https://doi.org/10.1109/TIE.2015.2405494.
[42] Li X, Li X, Ge SS, Khyam MO, Luo C. Automatic welding seam tracking and identification. IEEE Trans Ind Electron 2017;64:7261–71. https://doi.org/10.1109/TIE.2017.2694399.
[43] Schulenburg L. NDT 4.0: opportunity or threat? Mater Eval 2020;78:852–60. https://doi.org/10.32548/2020.me-04134.
[44] Vasilev M. Sensor-enabled robotics for ultrasonic NDE. PhD Thesis. University of Strathclyde; 2021.
[45] Vasilev M, MacLeod CN, Loukas C, Javadi Y, Vithanage RKW, Lines D, et al. Sensor-enabled multi-robot system for automated welding and in-process ultrasonic NDE. Sensors 2021;21. https://doi.org/10.3390/s21155077.
[46] National instrument-9214 16-channel temperature module n.d. https://www.ni.com/en-gb/support/model.ni-9214.html (accessed July 18, 2022).
[47] Ledbetter HM. Stainless-steel elastic constants at low temperatures. J Appl Phys 1981;52:1587–9. https://doi.org/10.1063/1.329644.
[48] Lee SS, Min U-S, Ahn B, Yoo SH. Elastic constants determination of thin cold-rolled stainless steels by dynamic elastic modulus measurements. J Mater Sci 1998;33:687–92. https://doi.org/10.1023/A:1004385611382.
[49] Sethian JA. Level set methods and fast marching methods: evolving interfaces in computational geometry, fluid mechanics, computer vision, and materials science. Cambridge University Press; 1999.
[50] Hassouna MS, Farag AA. Multi-stencils fast marching methods: a highly accurate solution to the eikonal equation on cartesian domains. IEEE Trans Pattern Anal Mach Intell 2007;29:1563–74. https://doi.org/10.1109/TPAMI.2007.1154.
[51] Popovici AM, Sethian JA. 3-D imaging using higher order fast marching traveltimes. Geophysics 2002;67:604–9. https://doi.org/10.1190/1.1468621.
[52] Rawlinson N, Sambridge M. Wave front evolution in strongly heterogeneous layered media using the fast marching method. Geophys J Int 2004;156:631–47. https://doi.org/10.1111/j.1365-246X.2004.02153.x.
[53] Sethian JA. Fast marching methods. SIAM Rev 1999;41:199–235. https://doi.org/10.1137/S0036144598347059.
[54] COMSOL 5.6 multiphysics reference manual n.d. https://doc.comsol.com/(accessed November 3, 2021).
[55] Micro-Epsilon Messtechnik. Compact laser scanner. Micro-Epsil Messtech n.d. https://www.micro-epsilon.co.uk (accessed July 19, 2022).
[56] Çengel YA, Ghajar AJ. Heat and mass transfer: fundamentals & applications. McGraw-Hill Education; 2019.
[57] Prabhu KMM. Window functions and their applications in signal processing. CRC Press; 2018.
[58] AMD ryzen threadripper 3960X desktop processor n.d. https://www.amd.com/en/products/cpu/amd-ryzen-threadripper-3960x (accessed July 20, 2022).
[59] Laugier P, Haïat G. Bone quantitative ultrasound. Springer Netherlands; 2010.
[60] Huthwaite P. Accelerated finite element elastodynamic simulations using the GPU. J Comput Phys 2014;257:687–707. https://doi.org/10.1016/j.jcp.2013.10.017.
[61] New Weld Series Probes. https://www.olympus-ims.com/en/probes/pa/weld-series/. accessed August 12, 2022.
[62] Ultrasonic phased array wedge for inspecting high-temperature parts n.d. https://www.olympus-ims.com/en/applications/ultrasonic-phased-array-wedge-for-inspecting-high-temperature-parts-up-to-150c/(accessed August 12, 2022).
[63] Rajagopal P, Drozdz M, Skelton EA, Lowe MJS, Craster RV. On the use of absorbing layers to simulate the propagation of elastic waves in unbounded isotropic media using commercially available Finite Element packages. NDT E Int 2012;51:30–40. https://doi.org/10.1016/j.ndteint.2012.04.001.
[64] Combaniere J, Cawley P, McAughey K, Giese J. Interaction between SH0 guided waves and tilted surface-breaking cracks in plates. IEEE Trans Ultrason Ferroelectrics Freq Control 2019;66:119–28. https://doi.org/10.1109/TUFFC.2018.2876723.
[65] De Luca A, Perfetto D, De Fenza A, Petrone G, Caputo F. Guided waves in a composite winglet structure: numerical and experimental investigations. Compos Struct 2019;210:96–108. https://doi.org/10.1016/j.compstruct.2018.11.048.
[66] Ma Y, Yang Z, Zhang J, Liu K, Wu Z, Ma S. Axial stress monitoring strategy in arbitrary cross-section based on acoustoelastic guided waves using PZT sensors. AIP Adv 2019;9:125304. https://doi.org/10.1063/1.5130723.
[67] Nvidia GeForce 3090 & 3090 Ti Graphics Cards. https://www.nvidia.com/en-gb/geforce/graphics-cards/30-series/rtx-3090-3090ti/. accessed August 15, 2022.
[68] MATLAB. Parallel Computing Toolbox. https://uk.mathworks.com/products/parallel-computing.html. accessed August 17, 2022.
[69] Intel Xeon Gold 6248R Processor Product Specifications. https://www.intel.com/content/www/us/en/products/sku/199351/intel-xeon-gold-6248r-processor-35-75m-cache-3-00-ghz.html. accessed August 15, 2022.
[70] MATLAB. GPU coder n.d. https://uk.mathworks.com/products/gpu-coder.html (accessed August 17, 2022).
[71] Lines D, Mohseni E, Zimermann R, Mineo C, MacLeod CN, Pierce G, et al. Modelling of echo amplitude fidelity for transducer bandwidth and TFM pixel resolution. 47th Annu Rev Prog Quant Nondestruct Eval, Virtual Event 2020.
[72] CREWES. https://www.crewes.org/. accessed November 22, 2022.
[73] Angle Probe Calculation for UT – welding & NDT. https://www.weldingandndt.com/angle-probe-calculation-for-ut/. accessed November 17, 2022.
[74] Kuka Kuka Industrial robots high payload catalogue n.d. https://www.kuka.com/-/media/kuka-downloads/imported/9cb8e311bfd744b4b0eab25ca883f6d3/kuka_pb_hohe_tl_en.pdf (accessed June 16 2022).
[75] Kuka KR 6 R900 n.d. https://www.kuka.com/-/media/kuka-downloads/imported/6b77eecacfe542d3b736af377562ecaa/0000205456_en.pdf (accessed August 17, 2022).
[76] ATI Industrial Automation. F/T Sensor Gamma IP65 n.d. https://www.ati-ia.com/products/ft/ft_models.aspx?id=Gamma+IP65 (accessed June 14 2022).
[77] Kuka. KRC4. https://www.kuka.com/en-gb/products/robotics-systems/robot-controllers/kr-c4. accessed June 16 2022.
[78] Kuka. System Software. https://www.kuka.com/en-us/products/robotics-systems/software/system-software/kuka_systemsoftware. accessed June 14 2022.
[79] Echo Ultrasonics. High temperature ultrasonic couplant n.d. https://www.echoultrasonics.com/product-category/high-temperature-ultrasonic-couplant/(accessed August 17, 2022).
[80] Peak NDT. LT-PA. https://www.peakndt.com/products/ltpa/. accessed August 15, 2022.